communications
physics

ARTICLE

https://doi.org/10.1038/s42005-023-01211-2 OPEN

Probing the optical near-field interaction of Mie nanoresonators with atomically thin semiconductors

Ana Estrada-Real[1,2]✉, Ioannis Paradisanos[2,3]✉, Peter R. Wiecha[4]✉, Jean-Marie Poumirol[5]✉, Aurelien Cuche[5], Gonzague Agez[5], Delphine Lagarde[2], Xavier Marie[2], Vincent Larrey[6], Jonas Müller[4], Guilhem Larrieu[4], Vincent Paillard[5] & Bernhard Urbaszek[1,2]✉

Optical Mie resonators based on silicon nanostructures allow tuning of light-matter-interaction with advanced design concepts based on complementary metal–oxide–semiconductor (CMOS) compatible nanofabrication. Optically active materials such as transition-metal dichalcogenide (TMD) monolayers can be placed in the near-field region of such Mie resonators. Here, we experimentally demonstrate and verify by numerical simulations coupling between a $MoSe_2$ monolayer and the near-field of dielectric nanoresonators. Through a comparison of dark-field (DF) scattering spectroscopy and photoluminescence excitation experiments (PLE), we show that the $MoSe_2$ absorption can be enhanced via the near-field of a nanoresonator. We demonstrate spectral tuning of the absorption via the geometry of individual Mie resonators. We show that we indeed access the optical near-field of the nanoresonators, by measuring a spectral shift between the typical near-field resonances in PLE compared to the far-field resonances in DF scattering. Our results prove that using $MoSe_2$ as an active probe allows accessing the optical near-field above photonic nanostructures, providing complementary information to sophisticated near-field microscopy equipment.

---

[1] Institute of Condensed Matter Physics, Technische Universität Darmstadt, 64289 Darmstadt, Germany. [2] Université de Toulouse, INSA-CNRS-UPS, LPCNO, 135 Avenue Rangueil, 31077 Toulouse, France. [3] Institute of Electronic Structure and Laser, Foundation of Research and Technology Hellas, 71110 Heraklion-Crete, Greece. [4] LAAS-CNRS, Université de Toulouse, 31000 Toulouse, France. [5] CEMES-CNRS, Université de Toulouse, Toulouse, France. [6] CEA-LETI, Université Grenoble-Alpes, Grenoble, France. ✉email: acarmen.ereal@gmail.com; iparad@iesl.forth.gr; pwiecha@laas.fr; jean-marie.poumirol@cemes.fr; bernhard.urbaszek@pkm.tu-darmstadt.de

Optical resonators are essential in many applications such as laser systems and sensing. The physical size and properties of the resonator are adapted to the specific application and to the relevant part of the electromagnetic spectrum[1]. Optical resonators that are capable of amplifying optical fields in very small nanoscopic volumes, for addressing individual nanocrystals or molecules in the near-field, are called nanoresonators[2–14]. They can be fabricated by bottom-up techniques, such as growth of metallic nanoparticles, or top-down approaches, such as Si-nanoresonators (Si-NRs) on CMOS compatible substrates[15–20]. Whereas the resonance energies of a resonator with macroscopic dimensions, such as a laser cavity, are directly accessible in a standard optical far-field measurement, the situation for nanoresonators is more challenging. It has been shown experimentally and in a substantial body of theory work that there is a shift between the optical resonance energy in the near-field compared to the measured resonance energies in the far-field. The exact near-field resonance is key for applications for example in sensing of molecules directly placed in the near-field[21] and it has been accessed up to now either in sophisticated tip-enhanced experiments (scanning near-field optical microscopy, SNOM), or through extrapolation from far-field data[22–26].

Here we show that by placing an atomically thin semiconductor directly in the near-field of individual dielectric nanoresonators, we have access to the near-field resonance energies without the use of complex near-field spectroscopy techniques. Our approach is thus particularly interesting for laboratories without direct access to SNOM equipment but with an existing, dedicated exfoliation experiment. We compare the near-field resonance energies with far-field resonance energy measurements on the same resonators and observe a clear blue-shift of the near-field energies in our far-field results. We show tuning of the optical absorption of the atomically thin semiconductor $MoSe_2$ through the interaction with the nanoresonator near-field and our results are well reproduced by model calculations of the shift between near-and far-field resonances. While the local field enhancement cannot be directly quantified with our approach, it nevertheless provides also qualitative information about the local field enhancement.

Results and discussion

We fabricated two sets of Si/SiO_2 nanoresonator arrays on silicon-on-insulator (SOI) substrates, see Supplementary Note 1. The nanoresonators are cylindrical pillars, arranged as close-packed heptamers as sketched in Fig. 1e, f. The diameters of the individual cylinders increase from 50 to 300 nm with steps of 50 nm. The gaps between neighboring pillars are 50, 100 or 300 nm. The structures are fabricated as arrays of seven discs to match approximately the size of a diffraction limited, focused laser beam, in order to maximize the experimental signal associated with the Si-NRs. On the final nanostructures, $MoSe_2$ monolayers are aligned and transferred on top of the nanoresonators using a micromanipulator system[27]. A description of the fabrication process is given in the Supporting Information, see also images in Supplementary Note 4.

In Fig. 1a, we show dark-field (DF) images of the nanoresonators before $MoSe_2$ transfer, Fig. 1c shows the same sample after transfer of an $MoSe_2$ monolayer flake. A bright-field microscope image of the nanoresonators after $MoSe_2$ deposition is shown in Supplementary Fig. S3, where the $MoSe_2$ covered region is clearly visible. By varying the Si-NR gap and diameter, different colors appear in the DF images, which demonstrates the geometry-dependent Mie resonance energy shifts of the individual resonators in the visible spectral range.

DF spectra are collected using the same setup as the DF images, see Supplementary Note 2. To this end, the signal is sent to a spectrometer instead of the imaging camera. The setup for taking dark-field images and spectra is depicted in Supplementary Fig. S1. We will focus in the following on two selected nanoresonators, “NR1” (blue, Fig. 1e) and “NR2” (red, Fig. 1f). These heptamers have respective diameters of 250 nm (NR1) and 300 nm (NR2), the gap between the pillars is identical for both Si-NRs (100 nm). We selected these two NRs because their main Mie resonances lie at different, well distinguishable energies. We measured the scattered light intensity before and after the monolayer transfer, shown in Fig. 1b,d, respectively. We observed a small, global blue-shift on the order of 10 meV for the resonances when the $MoSe_2$ monolayer was on top of the nanoresonators. This small energy-shift is at the limit of our detection accuracy and around a factor 5 smaller than the near-field resonance shift that we will discuss below. Knowing the size of this shift is helpful for analyzing the spectral shift between measured near-field and far-field resonances discussed below.

Spectral shift between near-field and far-field. In a second step, we want to analyze the impact of the nanoresonators on the absorption of the $MoSe_2$ monolayer. We carry out photoluminescence excitation (PLE) experiments[28] where temperature, position, and optical power (see details in Supplementary Note 5) are kept constant and the excitation wavelength is varied from 450 to 650 nm (corresponding to 2.75–1.90 eV). The optical power of the laser is set to 100 nW, after making sure that the $MoSe_2$ absorption is not saturated at this illumination power (see also Supplementary Fig. S4 and Supplementary Note 3). We avoid tuning the laser close to the $MoSe_2$ exciton emission peaks which occur around 745 nm (≈1.66 eV)[29–31], in order to remain in a non-resonant excitation regime. During the entire measurements, the sample is kept in a closed-loop cryostat at a temperature of 5 K, but we compare the results also to room temperature ($T = 300$K) measurements, which yield similar results (see below). An illustration of the optical setup can also be found in the Supplementary Fig. S2.

The absorption and hence the PLE response of the bare $MoSe_2$[28] is expected to vary with the excitation energy. This variation is a result of the material’s band-structure, the presence of high energy excitonic states as well as coupling to phonons[31–34]. Our goal is to investigate how the absorption is modified by Mie resonances of the Si-NRs. To distinguish effects induced by Mie-resonances from material-related variations in the bare $MoSe_2$, we compare PLE measurements from $MoSe_2$ monolayers lying on the flat substrate with $MoSe_2$ on top of the nanoresonators. This is shown in Fig. 2 for NR1 and NR2. The PL emission spectra for each excitation laser wavelength are numerically integrated, by summation of the counts per second in the spectral range around the emission peaks, from 1.5–1.7 eV (see Supplementary Fig. S5 SI for raw spectra)[35]. Hence, each data point in Fig. 2 is a separate PL measurement for a specific laser excitation energy. The direct comparison of the PLE measurements from $MoSe_2$ with and without Si-NR (c.f. Fig. 2), already reveals clear differences. To better visualize the effect of the nanoresonators on the PLE signal, we divide the integrated PL intensities from $MoSe_2$ on the Si-NRs $I_{PL,\mathrm{NR}}$ (blue squares and red triangles in Fig. 2) by the signal from the bare $MoSe_2 I_{PL,\mathrm{MoSe_2}}$ (on flat substrate, gray dotted line in Fig. 2):

$$\rho = \frac{I_{PL,\mathrm{NR}}}{I_{PL,\mathrm{MoSe_2}}}. \quad (1)$$

This ratio ρ gives an estimation of the absorption enhancement due to the presence of a nanoresonator supporting Mie resonances. The Mie resonances locally amplify the optical near-field, enhancing absorption in the monolayer which leads after carrier relaxation to a stronger PL emission.

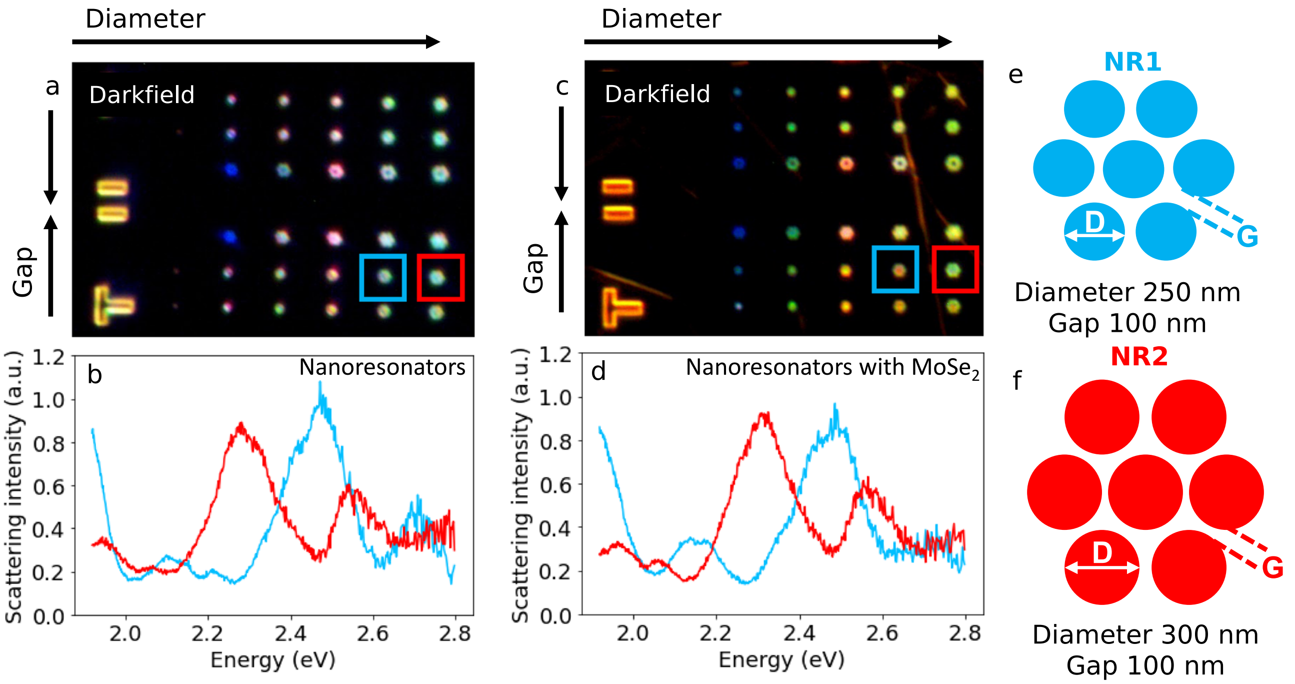

Fig. 1 Dark-field scattering images and spectra with and without $MoSe_2$. **a** Dark-field microscope image of SiO_2/Si nanoresonators, the 15 structures on the top part of the image are hexamers (six pillars) with diameters varying from $D = 100$–300 nm from left to right and the gap between pillars varying $G = 50$–100–300 nm from top to bottom. The 15 structures on the bottom are heptamers (seven pillars) with the same variation. **b** Dark-field scattering intensity of the two nanoresonators highlighted. **c** Dark-field microscope image with a $MoSe_2$ monolayer on top. Caution, automatic white-balance was used, colors do not directly compare to (**a**). **d** Dark-field scattering intensity of the two nanoresonators after transfer of $MoSe_2$ monolayer. **e**, **f** Sketches of the two selected nanoresonators NR1 and NR2, respectively (top view—see Supplementary Fig. S9 for side view).

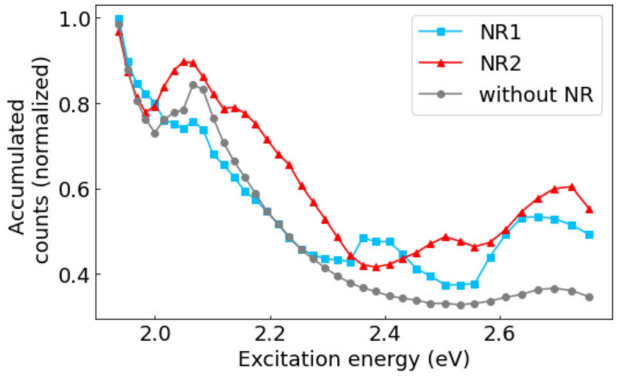

Fig. 2 Photoluminescence excitation measurements. Accumulated counts of the photoluminescence (PL) spectra measured on bare $MoSe_2$ (gray circles) and $MoSe_2$ on top of each nanoresonator NR1 (blue squares) and NR2 (red triangles), excited with a continuum laser at 40 different energies and at $T = 5$ K. See Supplementary Note 9 and Fig. S10 for laser energy tuning range.

In Fig. 3, we show a comparison of room temperature (RT) measurements (Fig. 3a) with PLE data from $T = 5$K (Fig. 3b), and compare both to the far-field scattering spectrum (Fig. 3c). In Fig. 3d, e we show selected PL spectra at RT and 5K, respectively. While the PL spectra are broadened at RT and the individual excitonic features (c.f. Fig. 3e) cannot be distinguished, the PLE spectra at RT are of similar quality as the ones obtained at cryogenic temperature. Further PL spectra from a reference without nanostructures are shown in Supplementary Fig. S5 in Supplementary Note 6, showing the impact of nanostructure induced strain on the PL spectra. We avoid significant impact of perturbations like strain on the PLE signal, by integrating the PL signal over the entire energy range (see also "Methods").

Spectra of ρ as a function of the excitation energy are shown in Fig. 4a. In order to show spectral tuning of the absorption enhanced by Mie-resonances we perform experiments on the two nanoresonators NR1 and NR2 (see Fig. 1e, f). We find that their main resonances (labeled RI, ..., RIV) occur at well separated energies (see Table 1 for values). Around the main Mie resonances we observe a PL emission enhancement of about 1.44. A comparison with the DF scattering spectrum (Fig. 4b) shows, that the PLE maxima are governed by the Mie-resonances. The spectral shifts between NR1 and NR2 are consistent between near- and far-field measurements. This is a clear signature that the $MoSe_2$ monolayer is coupled to the optical near-field above the Si-NR in the regime of weak coupling.

Theoretical simulations. We compare the experimental PLE spectra to full-field simulations via the Green's dyadic method (GDM) using our own python implementation "pyGDM"[36, 37]. The GDM is a volume discretization approach to solve Maxwell's equations in the frequency domain[38]. A nanostructure of arbitrary shape and material is discretized on a regular hexagonal compact grid. We use tabulated refractive indices from literature for both parts of the pillars, the first 95 nm consisting of silicon[39] while the 30 nm thick capping is made of SiO_2[40]. With according Green's tensors[41], we describe the layered substrate, where a bulk silicon substrate is followed by a SiO_2 spacer layer of 145 nm, on top of which the nano-structures are placed in air. We illuminate the system with a plane wave at normal incidence in the same wavelength range as used in the experiments and we incoherently average two orthogonal linear polarizations. We calculate the electric field intensity enhancement just above the SiO_2 capping on the Si pillars in an area of $1 \times 1\,\mu m^2$, corresponding approximately to the size of the focused Gaussian laser beam (≈emission beam diameter). Sketches and more details about simulations and model geometry can be found in the Supplement.

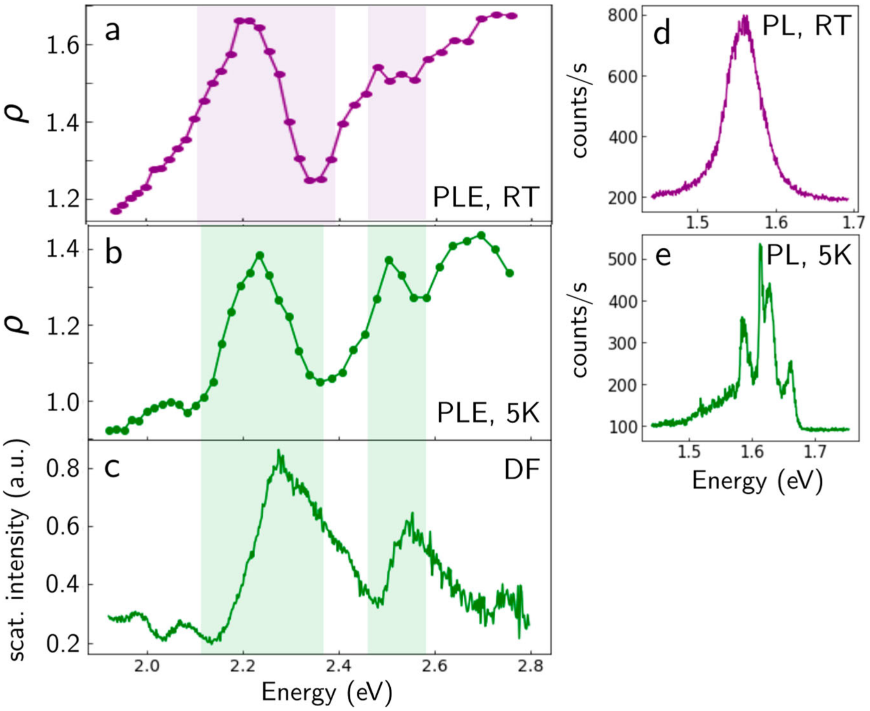

Fig. 3 Room temperature vs. $T = 5$K. PLE spectrum measured at (**a**) room temperature ($T = 300$K) and (**b**) cryogenic temperature ($T = 5$K) as well as (**c**) dark-field scattering, all from NR2. See Supplementary Note 10 with Fig. S11 for additional measurements on a different resonator (NR3). **d**, **e** show the PL spectrum at room temperature, respectively $T = 5$K under excitation at $E_{\mathrm{laser}} = 2.47$ eV. The two main Mie resonances are highlighted by a colored background.

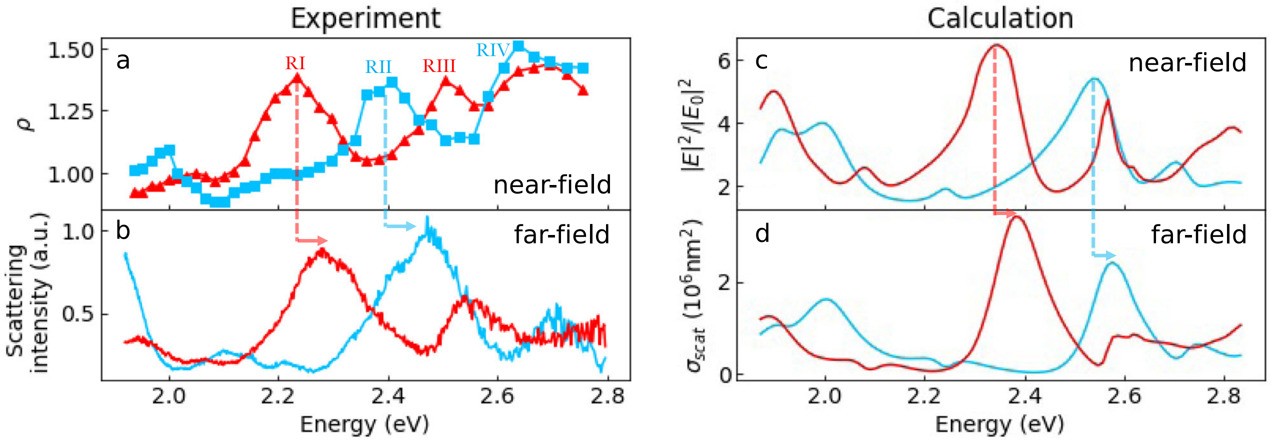

Fig. 4 Tuning of resonances and spectral shift. Results of measurements and calculations for NR1 and NR2. **a** The result of dividing PLE over NR1 (blue squares) and NR2 (red triangles) by PLE on bare $MoSe_2$, where we plot the ratio ρ as defined in Eq. (1) (data obtained under $T = 5$K). **b** Dark-field scattering intensity, same data as Fig. 1b. **c** Calculated near-field intensity enhancement above the Si-NRs, averaged in the plane of the TMD. **d** Calculated far-field scattering cross section. In the Supplementary see Note 7 and Figs. S6–S8 for further details on simulations.

Table 1 Energy of measured resonances, where we compare near-field (PLE) with far-field (dark-field scattering) experiments.

	RI (eV)	RII (eV)	RIII (eV)	RIV (eV)
PLE	2.23 ± 0.05	2.41 ± 0.05	2.50 ± 0.05	2.64 ± 0.05
Dark-field	2.28 ± 0.01	2.46 ± 0.01	2.54 ± 0.01	2.71 ± 0.01

Resonance labels according to Fig. 4a.

The simulated spectra of the average near-field enhancement above the top surface are shown in Fig. 2c Fig. 4c for heptamers with pillar diameters of $D = 250$ nm (NR1, blue) and $D = 300$ nm (NR2, red), and the far-field scattered intensity for the same structures shown in Fig. 2d Fig. 4d. We observe a good agreement with the experimental data, the simulations reproduce in particular all major resonance features. Very importantly our simulations reproduce the red-shift of the resonances when the structure size increases from $D = 250$ nm to $D = 300$ nm and the near-to far-field shift. Please note that we observe a systematic blue-shift of around $0.05 - 0.1$ eV between the absolute values of the simulated resonance energies and the experimental results. To investigate this shift we perform scanning electron microscopy (SEM) on the heptamers, where we find that the fabricated structures are systematically smaller by around 3-4% compared to the target size, as shown in Supporting Information Fig. S12. We suppose that this size discrepancy as well as the relatively rough discretization of the Si discs' circular cross-sections in our simulations, are responsible for the observed shift between experiment and simulations (c.f. refs. [16, 42]).

Discussion. The comparison of the far-field DF scattering spectra with the $MoSe_2$ PLE spectra clearly demonstrate, that the Mie resonances of high-index dielectric nanoresonators can be used to tailor the absorption of a TMD layer. Furthermore, our results show that the PLE measurements access the optical near-field and probe the local field intensity enhancement. In the lateral directions (parallel to the substrate plane) the measurements qualitatively reflect the average near-field intensity in a large zone, corresponding approximately to the illuminated area. Perpendicular to the surface on the other hand, the local near-field is probed in an extremely narrow vertical region, because the TMD is atomically thin.

However, the PL signal is significantly lower than the simulated near-field enhancements. This is due to the fact that we measure photoluminescence intensity as a result of absorption in the monolayer, but we simulate the near-field intensity enhancement. We show in Supporting Information Fig. S4, that the PL signal provides only a lower bound for the absorption in the TMD (the generated excitons do not all recombine radiatively). Furthermore, the absorption in the flat monolayer is likely to depend on the local electric field vector's orientation, our simulations however show the total field intensity. Also, the absorption increases not necessarily linearly. Close to saturation, it will even stop increasing with the local field amplitude[43]. Further effects like the averaging over the beam spot size also intervene.

An unambiguous proof that we do indeed probe the optical near-field with the PLE technique is provided by the observation of a systematic shift between near-field spectra (PLE) and far-field measurements (DF scattering). This shift is of the order of 50 meV (see also Table 1) and is reproduced by our simulations (Fig. 4c, d). It corresponds to the widely studied resonance shift between far-field and near-field, where the near-field amplitude is shifted to lower energies, compared to the far-field response. To get an intuitive, qualitative understanding, this shift can be explained with a damped harmonic oscillator (HO) model. The HO amplitude is given by:

$$A(\omega) = \frac{A_{\mathrm{drive}}}{\sqrt{\left(1-(\omega/\omega_0)^2\right)^2 + \gamma^2 (\omega/\omega_0)^2}}, \qquad (2)$$

where A_{drive} is the driving amplitude, in our case corresponding to the amplitude of the incident field. Solving Eq. (2) for its extrema, one finds easily that the damping term γ leads to a red-shift of the maximum resonator amplitude $\omega_{A_{\max}}$ with respect to the eigenfrequency ω_0[25]:

$$\omega_{A_{\max}} = \omega_0 \sqrt{1-\gamma^2/2}. \qquad (3)$$

On the other hand, far-field observables like the scattering or extinction cross section are proportional to the oscillator's kinetic energy, whose time average can be shown to be maximum at the non-shifted eigenfrequency ω_0[25]. While the effect has first been discussed for lossy plasmonic nanoresonantors[22], it has been explicitly shown later that radiative damping, responsible for broadening of leaky Mie resonances like in our Si-NRs, leads to an analogous near-field shift[25]. The shift has been experimentally demonstrated on plasmonic structures via scanning near-field microscopy (SNOM) measurements[26].

Without complex SNOM equipment, here we experimentally observe a red-shift of the PLE spectra compared to the far-field scattering results. It is on the order of the shift predicted by our near-field enhancement simulations, and therefore a clear signature that we indeed probe the optical near-field of the silicon nanostructures.

These observations rely on a sufficient spectral resolution to observe the near-field red-shift in the PLE data. While the PLE energy resolution seems to be slightly better at cryogenic temperatures, please note that our approach also works well at room temperature (see Fig. 3).

In conclusion, we transferred monolayers of $MoSe_2$ on top of Mie resonant silicon nanostructure arrays and compared the far-field scattering of these scatterers, using DF spectroscopy, with spectrally resolved measurements of photoluminescence enhancement. The latter is probing the optical near-field at the location of the TMD monolayer, i.e., just above the silicon nanostructures. We found that the PLE spectra show the same resonant features as the far-field measurements. We also observe the typical near-to-far-field spectral shift between the two types of measurements, which unambiguously confirms that we have access to the optical near-field of the silicon nanostructures. All results are confirmed by numerical full-field simulations. Our results demonstrate that the absorption efficiency and consequently the emission of direct-bandgap monolayer semiconductors can be enhanced and spectrally tuned by placing optically resonant nanostructures in their vicinity. It furthermore proves that the PLE measurements provide access to the optical near-field in an extremely narrow vertical region in the order of a nanometer (thickness of the TMD monolayer). Our work offers important insights for the design of efficient TMD-based nano-devices for light detection and emission.

Methods

The silicon pillars were fabricated in a top-down approach via electron-beam lithography (EBL) and subsequent anisotropic plasma etching[44, 45]. See Supplementary Notes 8 and 11 with Figs. S9 and S12 for further details on the sample geometry and fabrication (electron microscopy). Monolayer $MoSe_2$ flakes are exfoliated from bulk 2H-$MoSe_2$ crystals on Nitto Denko tape[46] and then exfoliated again on a polydimethylsiloxane (PDMS) stamp placed on a glass slide for inspection under the optical microscope, see supplement for further details.

The PL emission features of the TMD monolayers depend on strain and localization[47–50]. This leads to not one simple excitonic emission peak but up to four different peaks when measured on top of the nanoresonators. Our approach is to integrate the emission over all these emission peaks in our PLE experiments in order to access absorption. First step: we consider that the laser at high energy generates electron-holes pairs and our target is to measure how many electron-hole pairs have been generated. Second step: excitons relax in energy and go to regions with different strain, possibly forming charged excitons if residual carriers are present. At what exact energy these excitons emit depends on the energy relaxation processes which are rather complex and involve phonons and transfers between charged and neutral excitons. But we want to access the global exciton population generated at high energy, so integrating the entire PL emission spectrum is the most direct access we can have to this information.

We take the global, integrated PL emission intensity as a probe for absorption, so high integrated PL signal for a certain laser wavelength corresponds to a large number of excitons created. The agreement between PLE and DF resonances is striking, showing that our experimental approach indeed reflects the absorption properties. Although the PL spectra at cryogenic temperature are different compared to room temperature (due to broadening by phonons and other processes) the comparison between PLE and DF works for both sets of experiments, which validates our approach.

Data availability

The data that support the findings of this study are available from the corresponding authors upon request.

Received: 8 February 2023; Accepted: 19 April 2023;
Published online: 11 May 2023

References

1. Novotny, L. & Hecht, B. *Principles of Nano-optics* (Cambridge University Press, 2012).
2. Kleemann, M.-E. et al. Strong-coupling of WSe_2 in ultra-compact plasmonic nanocavities at room temperature. *Nat. Commun.* **8**, 1–7 (2017).
3. Petric, M. M. et al. Tuning the optical properties of a $MoSe_2$ monolayer using nanoscale plasmonic antennas. *Nano Lett.* **22**, 561–569 (2022).
4. Liu, W. et al. Strong exciton–plasmon coupling in MoS_2 coupled with plasmonic lattice. *Nano Lett.* **16**, 1262–1269 (2016).
5. Zhou, Y. et al. Probing dark excitons in atomically thin semiconductors via near-field coupling to surface plasmon polaritons. *Nat. Nanotechnol.* **12**, 856–860 (2017).
6. Sortino, L. et al. Enhanced light-matter interaction in an atomically thin semiconductor coupled with dielectric nano-antennas. *Nat. Commun.* **10**, 1–8 (2019).
7. Bidault, S., Mivelle, M. & Bonod, N. Dielectric nanoantennas to manipulate solid-state light emission. *J. Appl. Phys.* **126**, 094104 (2019).
8. Mupparapu, R., Bucher, T. & Staude, I. Integration of two-dimensional transition metal dichalcogenides with mie-resonant dielectric nanostructures. *Adv. Phys. X* **5**, 1734083 (2020).
9. Brongersma, M. L. The road to atomically thin metasurface optics. *Nanophotonics* **10**, 643–654 (2021).
10. Chen, H. et al. Enhanced directional emission from monolayer WSe_2 integrated onto a multiresonant silicon-based photonic structure. *ACS Photonics* **4**, 3031–3038 (2017).
11. Bucher, T. et al. Tailoring photoluminescence from MoS_2 monolayers by mie-resonant metasurfaces. *ACS Photonics* **6**, 1002–1009 (2019).
12. Cihan, A. F., Curto, A. G., Raza, S., Kik, P. G. & Brongersma, M. L. Silicon mie resonators for highly directional light emission from monolayer MoS_2. *Nat. Photonics* **12**, 284–290 (2018).
13. Shinomiya, H. et al. Enhanced light emission from monolayer MoS_2 by doubly resonant spherical si nanoantennas. *ACS Photonics* **9**, 1741–1747 (2022).
14. Poumirol, J.-M. et al. Unveiling the optical emission channels of monolayer semiconductors coupled to silicon nanoantennas. *ACS Photonics* **7**, 3106–3115 (2020).
15. Zhao, Q., Zhou, J., Zhang, F. & Lippens, D. Mie resonance-based dielectric metamaterials. *Mater. Today* **12**, 60–69 (2009).
16. Wiecha, P. R. et al. Evolutionary multi-objective optimization of colour pixels based on dielectric nanoantennas. *Nat. Nanotechnol.* **12**, 163–169 (2017).
17. Won, R. Into the 'mie-tronic' era. *Nat. Photonics* **13**, 585–587 (2019).
18. Gonzalez-Zalba, M. et al. Scaling silicon-based quantum computing using cmos technology. *Nat. Electron.* **4**, 872–884 (2021).
19. Kuznetsov, A. I., Miroshnichenko, A. E., Brongersma, M. L., Kivshar, Y. S. & Luk'yanchuk, B. Optically resonant dielectric nanostructures. *Science* **354**, aag2472 (2016).
20. Kallel, H. et al. Photoluminescence enhancement of silicon nanocrystals placed in the near field of a silicon nanowire. *Phys. Rev. B* **88**, 081302 (2013).
21. Chen, X. et al. Modern scattering-type scanning near-field optical microscopy for advanced material research. *Adv. Mater.* **31**, 1804774 (2019).
22. Messinger, B. J., von Raben, K. U., Chang, R. K. & Barber, P. W. Local fields at the surface of noble-metal microspheres. *Phys. Rev. B* **24**, 649–657 (1981).
23. Ross, B. M. & Lee, L. P. Comparison of near- and far-field measures for plasmon resonance of metallic nanoparticles. *Opt. Lett.* **34**, 896–898 (2009).
24. Kats, M. A., Yu, N., Genevet, P., Gaburro, Z. & Capasso, F. Effect of radiation damping on the spectral response of plasmonic components. *Opt. Express* **19**, 21748–21753 (2011).
25. Zuloaga, J. & Nordlander, P. On the energy shift between near-field and far-field peak intensities in localized plasmon systems. *Nano Lett.* **11**, 1280–1283 (2011).
26. Alonso-González, P. et al. Experimental verification of the spectral shift between near- and far-field peak intensities of plasmonic infrared nanoantennas. *Phys. Rev. Lett.* **110**, 203902 (2013).
27. Castellanos-Gomez, A. et al. Deterministic transfer of two-dimensional materials by all-dry viscoelastic stamping. *2D Mater.* **1**, 011002 (2014).
28. Shree, S., Paradisanos, I., Marie, X., Robert, C. & Urbaszek, B. Guide to optical spectroscopy of layered semiconductors. *Nat. Rev. Phys.* **3**, 39–54 (2021).
29. van der Zande, A. M. et al. Grains and grain boundaries in highly crystalline monolayer molybdenum disulphide. *Nat. Mater.* **12**, 554–561 (2013).
30. Cadiz, F. et al. Ultra-low power threshold for laser induced changes in optical properties of 2D molybdenum dichalcogenides. *2D Mater.* **3**, 045008 (2016).
31. Wang, G. et al. Exciton states in monolayer $MoSe_2$: impact on interband transitions. *2D Mater.* **2**, 045005 (2015).
32. Chow, C. M. et al. Phonon-assisted oscillatory exciton dynamics in monolayer mose2. *npj 2D Mater. Appl.* **1**, 1–6 (2017).
33. Kozawa, D. et al. Evidence for fast interlayer energy transfer in $MoSe_2/WS_2$ heterostructures. *Nano Lett.* **16**, 4087–4093 (2016).
34. Shree, S. et al. Observation of exciton-phonon coupling in $MoSe_2$ monolayers. *Phys. Rev. B* **98**, 035302 (2018).
35. Atkinson, K. E. *An Introduction to Numerical Analysis* (John Willey & Sons, 1989).
36. Wiecha, P. R. pygdm—a python toolkit for full-field electro-dynamical simulations and evolutionary optimization of nanostructures. *Comput. Phys. Commun.* **233**, 167–192 (2018).
37. Wiecha, P. R. et al. pyGDM—new functionalities and major improvements to the python toolkit for nano-optics full-field simulations. *Comput. Phys. Commun.* **270**, 108142 (2022).
38. Girard, C. Near fields in nanostructures. *Rep. Prog. Phys.* **68**, 1883–1933 (2005).
39. Edwards, D. F. Silicon (Si)*. In *Handbook of Optical Constants of Solids* (ed. Palik, E. D.) 547–569 (Academic Press, 1997).
40. Malitson, I. H. Interspecimen comparison of the refractive index of fused silica. *J. Opt. Soc. Am.* **55**, 1205 (1965).
41. Paulus, M., Gay-Balmaz, P. & Martin, O. J. F. Accurate and efficient computation of the Green's tensor for stratified media. *Phys. Rev. E* **62**, 5797–5807 (2000).
42. Patoux, A. et al. Challenges in nanofabrication for efficient optical metasurfaces. *Sci. Rep.* **11**, 1–12 (2021).
43. Majorel, C., Girard, C., Cuche, A., Arbouet, A. & Wiecha, P. R. Quantum theory of near-field optical imaging with rare-earth atomic clusters. *JOSA B* **37**, 1474–1484 (2020).
44. Han, X.-L., Larrieu, G., Fazzini, P.-F. & Dubois, E. Realization of ultra dense arrays of vertical silicon nanowires with defect free surface and perfect anisotropy using a top-down approach. *Microelectron. Eng.* **88**, 2622–2624 (2011).
45. Guerfi, Y., Carcenac, F. & Larrieu, G. High resolution HSQ nanopillar arrays with low energy electron beam lithography. *Microelectron. Eng.* **110**, 173–176 (2013).
46. Novoselov, K. S. et al. Two-dimensional atomic crystals. *Proc. Natl Acad. Sci. USA* **102**, 10451–10453 (2005).
47. Branny, A., Kumar, S., Proux, R. & Gerardot, B. D. Deterministic strain-induced arrays of quantum emitters in a two-dimensional semiconductor. *Nat. Commun.* **8**, 15053 (2017).
48. Branny, A. et al. Discrete quantum dot like emitters in monolayer $MoSe_2$: spatial mapping, magneto-optics, and charge tuning. *Appl. Phys. Lett.* **108**, 142101 (2016).
49. Montblanch, A. R.-P. et al. Confinement of long-lived interlayer excitons in WS_2/WSe_2 heterostructures. *Commun. Phys.* **4**, 1–8 (2021).
50. Yu, L. et al. Site-controlled quantum emitters in monolayer $MoSe_2$. *Nano Lett.* **21**, 2376–2381 (2021).

Acknowledgements

We acknowledge partial funding from ANR HiLight, NanoX project 2DLight, the Institute of Quantum Technology in Occitanie IQO and a UPS excellence PhD grant. This work was supported by the Toulouse HPC CALMIP (grant p20010), and by the LAAS-CNRS micro and nanotechnologies platform, a member of the French RENATECH network. I.P. acknowledges financial support by the Hellenic Foundation for Research and Innovation (H.F.R.I.) under the "3rd Call for H.F.R.I. Research Projects to support Post-Doctoral Researchers" (Project Number: 7898).

Author contributions

V.L. fabricated the high quality Si-SiO_2 starting structure. J.M. and G.L. fabricated the nanoresonators based on the design of A.C., G.A. and V.P. A.E.-R. and I.P. deposited the TMD layer on the nanoresonators. A.E.-R., P.R.W. and J.-M.P. performed dark-field experiments that were analyzed with all co-authors. D.L. and X.M. mounted the laser system for PLE. A.E.-R. performed PLE and analyzed data with I.P. P.R.W., A.E.-R., G.A. and A.C. performed modeling of the resonances. A.E.-R. wrote the manuscript with input from all co-authors. V.P., G.L., P.R.W. and B.U. supervised the project.

Funding

Open Access funding enabled and organized by Projekt DEAL.

Competing interests

The authors declare no competing interests.

Additional information

Supplementary information The online version contains supplementary material available at https://doi.org/10.1038/s42005-023-01211-2.

Correspondence and requests for materials should be addressed to Ana Estrada-Real, Ioannis Paradisanos, Peter R. Wiecha, Jean-Marie Poumirol or Bernhard Urbaszek.

Peer review information *Communications Physics* thanks the anonymous reviewers for their contribution to the peer review of this work. Peer reviewer reports are available.

Reprints and permission information is available at http://www.nature.com/reprints

Publisher's note Springer Nature remains neutral with regard to jurisdictional claims in published maps and institutional affiliations.

Open Access This article is licensed under a Creative Commons Attribution 4.0 International License, which permits use, sharing, adaptation, distribution and reproduction in any medium or format, as long as you give appropriate credit to the original author(s) and the source, provide a link to the Creative Commons license, and indicate if changes were made. The images or other third party material in this article are included in the article's Creative Commons license, unless indicated otherwise in a credit line to the material. If material is not included in the article's Creative Commons license and your intended use is not permitted by statutory regulation or exceeds the permitted use, you will need to obtain permission directly from the copyright holder. To view a copy of this license, visit http://creativecommons.org/licenses/by/4.0/.

© The Author(s) 2023